Catalysis Science & Technology

PAPER

View Article Online
View Journal | View Issue

Cite this: *Catal. Sci. Technol.*, 2017, 7, 607

Insights into the catalytic cycle and activity of methanol-to-olefin conversion over low-silica AlPO-34 zeolites with controllable Brønsted acid density

Weili Dai,[ab] Ge Cao,[a] Liu Yang,[a] Guangjun Wu,[ab] Michael Dyballa,[c] Michael Hunger,[c] Naijia Guan[ab] and Landong Li*[ab]

Received 8th December 2016,
Accepted 4th January 2017

DOI: 10.1039/c6cy02564a

www.rsc.org/catalysis

Low-silica AlPO-34 materials with similar crystal sizes but different Brønsted acid site densities were prepared and investigated as catalysts in methanol-to-olefin (MTO) conversion. The effect of Brønsted acid site density on catalyst activity and the dominant reaction mechanism during the MTO conversion was investigated *via* TGA, GC-MS, solid-state NMR spectroscopy, and *in situ* UV/vis spectroscopy together with the catalytic performance. For the catalysts with lower Brønsted acid site densities, the olefin-based cycle mechanism is the dominant mechanism during the MTO conversion. Long-chain alkenes, *e.g.*, $C_5^=$–$C_6^=$ alkenes, act as intermediates that are cracked to lower olefins, or are converted to dienes *via* hydride transfer reactions, and can also diffuse out of the cages of low-silica AlPO-34 catalysts as the products. With decreasing Brønsted acid site density or reaction temperature, the methylation route of the olefin-based cycle was found to be much more favored than the cracking route. Therefore, a higher selectivity to $C_5^=$–$C_6^=$ alkenes (~50%) is achieved. Simultaneously, dienes are the predominant deposits occluded in the used catalysts. For catalysts with slightly higher Brønsted acid site densities, the long-chain alkenes are rapidly transformed to aromatics and, subsequently, an aromatic-based cycle mechanism contributes to the MTO conversion. Interestingly, the catalyst with the most suitable Brønsted acid site density can well balance the above-mentioned two reaction cycles accompanied by a low deactivation rate, leading to a long catalyst lifetime of up to 15 h.

1. Introduction

As a potential route for producing olefins, methanol-to-olefin (MTO) conversion over solid acid catalysts has attracted extensive attention.[1–6] Over the past decades, a variety of acidic microporous catalysts have been studied as possible MTO catalysts.[2,7–12] Among these catalysts, silicoaluminophosphate SAPO-34 (CHA) with chabazite cages and 8-ring windows is the most interesting candidate for application as the shape-selective acidic catalyst in the MTO conversion. Extensive work has been focused on the catalytic and mechanistic aspects of the MTO conversion on SAPO-34.[13–19] According to the well accepted hydrocarbon pool mechanism proposed by Dahl and Kolboe, polyalkyl aromatics and their protonated forms confined inside the cages of SAPO-34 are the active reaction intermediates leading to the formation of light olefins upon activation by Brønsted acid sites at the framework.[13–19] Recently, a dual-cycle mechanism was proposed by the Olsbye group based on the hydrocarbon pool mechanism, and alkenes were considered as another type of active hydrocarbon pool species.[20,21] Subsequently, great attention has been paid to adapting and extending this dual-cycle mechanism to different zeolite catalysts *via* experimental and theoretical work.[22–32]

Considering that olefins and aromatics can simultaneously exist in zeolite pores, the corresponding olefin- and aromatic-based cycles should operate in a competitive relation. Recently, it has been indicated that the aromatic-based cycle can be suppressed in H-ZSM-22 zeolites with one-dimensional 10-ring pores, and higher alkenes were detected as the main products.[33–35] In contrast, for H-ZSM5 zeolites with 2-dimensional 10-ring pores, the two reaction cycles are not isolated from one another, and both contribute to the MTO conversion.[23] Interestingly, Ahn *et al.*[36] and Simonetti *et al.*[37] indicated that the olefin-based cycle can be selectively

[a] *School of Materials Science and Engineering & National Institute for Advanced Materials, Nankai University, Tianjin 300350, P.R. China. E-mail: lild@nankai.edu.cn*
[b] *Key Laboratory of Advanced Energy Materials Chemistry of the Ministry of Education, Collaborative Innovation Center of Chemical Science and Engineering, Nankai University, Tianjin 300071, P.R. China*
[c] *Institute of Chemical Technology, University of Stuttgart, 70550 Stuttgart, Germany*

favored over the aromatic-based cycle by altering the reaction conditions in H-Beta zeolites with 12-ring pores. Recent theoretical studies of Wang *et al.* demonstrated that olefins themselves are likely to be the dominant hydrocarbon pool species in the SAPO-34 zeolite.[28] Our recent investigations also indicated that the olefin-based cycle is the dominant reaction mechanism during the initial stages of the MTO conversion over SAPO-34.[38] However, with the rapid formation of aromatics, the aromatic-based cycle may start to participate in the steady-state of the MTO conversion. Very recent studies of Bhan and co-workers extended the dual-cycle mechanism over SAPO-34 *via* isotopic tracer studies.[24] Additionally, the olefin-based cycle was disclosed as the dominant mechanism during the early stages of MTO conversion over SAPO-41 and SAPO-5 with 1-dimensional pores and weak Brønsted acid sites.[39–41]

As is well known, MTO conversion is an acid-catalyzed reaction, that is, Brønsted acid sites play a key role as catalytically active sites in this process.[42] On one side, the initial intermediates in the olefin-based cycle, *e.g.*, alkenes and carbenium ions, even the dienes, can be formed at the Brønsted acid sites of the zeolite catalysts during the early stages of the MTO conversion. On the other side, the large compounds in the aromatic-based cycle, namely polymethylbenzene, even the polycyclic aromatics, can also be rapidly formed at the Brønsted acid sites, which can lead to deactivation of the MTO catalysts eventually. Therefore, significant attention has been paid to controlling the Brønsted acid sites to reduce the deactivation ratio and prolong the catalyst lifetime.[43–46] Up to now, however, it is still not clear, whether the Brønsted acid site density can influence the dual-cycle mechanism over SAPO-34 or whether it is possible to suppress the aromatic-based cycle and to effectively alter the contents of the two reaction cycles during the MTO conversion, which is the main goal of the present work.

Generally, the Brønsted acidity of SAPO zeolites is caused by bridging OH groups (Si(OH)Al), *i.e.* by hydroxyl protons compensating the unbalanced negative charges due to the Si incorporation into the neutral AlPO framework.[47] Hence, adjustment of the silicon content during the synthesis procedure is a suitable approach to modify the Brønsted acid site density of SAPO-34. However, according to previous studies of Liu and coworkers,[47] SAPO-34 with the CHA structure could not be obtained when the SiO_2/Al_2O_3 molar ratio in the starting gel was lower than 0.075. Fortunately, our previous studies demonstrated that the introduction of traces of silicon during the synthesis process of AlPO-34 can create correspondingly low Brønsted acid site densities.[42,48] Initiated by these earlier studies, a series of low-silica AlPO-34 materials with different Brønsted acid site densities were prepared and investigated as catalysts in the MTO conversion. The effect of the Brønsted acid site density of these materials on their catalytic performance and the dominant reaction mechanism during the MTO conversion was investigated in detail *via* TGA, GC-MS, solid-state NMR spectroscopy, and *in situ* UV/vis spectroscopy.

2. Experimental section

2.1 Catalyst preparation

The low-silica AlPO-34 materials were synthesized *via* a hydrothermal route from a molar gel composition of $x SiO_2 : 1.0Al_2O_3 : 1.0P_2O_5 : 2.5$ morpholine : $0.7HF : 100H_2O$, where x was equal to 0, 0.01, 0.02, 0.05 and 0.1, leading to the sample assignments A-0, A-0.01, A-0.02, A-0.05, and A-0.1, respectively. The detailed chemical compositions of the synthesis mixtures and the conditions for the synthesis of different low-silica AlPO-34 materials are summarized in Table 1. In a typical synthesis, orthophosphoric acid solution (85 wt%) and pseudo-boehmite as the aluminum source were mixed with distilled water and stirred for 2 h, followed by dropwise addition of the structure-directing agent morpholine (Mor). Thereafter, silica sol as the silica source was added dropwise. Then, HF (25%) was added and the mixture was further stirred for 6 h at room temperature, and the formed gel was transferred into a Teflon-lined stainless-steel autoclave for static crystallization. After crystallization at the temperature and duration given in Table 1 (columns 3 and 4), the solid products were separated by using a centrifuge, washed four times with demineralized water, and dried at 353 K for 12 h.

2.2 Catalyst characterization

X-ray diffraction (XRD) patterns of the prepared materials before and after calcination were recorded on a Bruker D8 diffractometer with CuKα radiation (λ = 1.5418 Å) at 5–50°.

The crystal morphologies of the as-synthesized samples were studied using a JEOL-JSM7500 field emission scanning electron microscope (FESEM). The SEM images were recorded after covering the samples with a thin layer of gold, deposited by sputtering.

The chemical compositions of the calcined AlPO-34 samples were determined by using an inductively coupled plasma atomic emission spectrometer (ICP-AES, IRIS Advantage). The surface areas of the calcined AlPO-34 materials were obtained by means of nitrogen adsorption at 77 K in a Quantachrome Autosorb 3B instrument. Before the nitrogen adsorption, the samples were dehydrated at 473 K for 2 h. The total surface areas were calculated *via* the Brunauer–Emmett–Teller (BET) equation.

The solid-state NMR investigations of the Brønsted acid sites and the catalyst framework were performed using a Bruker Avance III 400WB spectrometer at resonance frequencies of 400.3, 104.3, 79.5, and 161.9 MHz for ^{1}H, ^{27}Al, ^{29}Si, and ^{31}P nuclei, respectively. The MAS spectra were recorded upon single pulse excitation of $\pi/2$ for ^{1}H, ^{29}Si, and ^{31}P and $\pi/6$ for ^{27}Al nuclei with repetition times of 10 s for ^{1}H, 20 s for ^{29}Si, 0.5 s for ^{27}Al, and 30 s for ^{31}P nuclei. Sample spinning rates of 8 kHz for ^{1}H, ^{27}Al, and ^{31}P nuclei and 4 kHz for ^{29}Si nuclei were used. To avoid hydrolysis of the AlPO-34 framework, hydration of the samples under study was performed not longer than one day before the NMR characterization by exposing the samples to an atmosphere saturated with the vapor of a 1 M aqueous solution of $Ca(NO_3)_2$ at

Table 1 Parameters used for the synthesis of low-silica AlPO-34 samples with different silicon contents

Samples	Molar composition	Temperature (K)	Time (day)
A-0	$1.0Al_2O_3 : 1.0P_2O_5 : 2.5Mor : 1.0HF : 100H_2O$	463	5
A-0.01	$0.01SiO_2 : 1.0Al_2O_3 : 1.0P_2O_5 : 2.5Mor : 1.0HF : 100H_2O$	463	5
A-0.02	$0.02SiO_2 : 1.0Al_2O_3 : 1.0P_2O_5 : 2.5Mor : 1.0HF : 100H_2O$	463	5
A-0.05	$0.05SiO_2 : 1.0Al_2O_3 : 1.0P_2O_5 : 2.5Mor : 1.0HF : 100H_2O$	463	5
A-0.1	$0.1SiO_2 : 1.0Al_2O_3 : 1.0P_2O_5 : 2.5Mor : 1.0HF : 100H_2O$	463	5

ambient temperature. Before the ^1H MAS NMR experiments, the samples were completely dehydrated in a vacuum (pressure below 10^{-2} Pa) at the temperature of 673 K for 10 h.

2.3 Catalytic investigations

The MTO conversion was performed in a fixed-bed reactor at atmospheric pressure, as described in our previous work.[38] Typically, a 0.4 g sample with the sieve fraction of 0.25–0.5 mm was placed in a stainless steel reactor (5 mm i.d.) and activated under flowing N_2 at 723 K for 1 h, and then decreased to the desired reaction temperature. The reaction products were analyzed by using an on-line gas chromatograph equipped with a flame ionization detector and a capillary column Plot Q to separate the reaction products. The temperature of the column was maintained at 313 K for 7 min, increased to 473 K with a rate of 10 K min^{-1}, and then maintained at 473 K for 4 min.[39]

2.4 *In situ* and *ex situ* UV/vis studies of the MTO conversion on the low-silica AlPO-34 catalysts

The nature of organic intermediates formed on the catalysts during the MTO conversion was *in situ* monitored by UV/vis spectroscopy, as described in our previous work.[37] After stopping the MTO conversion, the organic compounds occluded inside the catalysts were investigated by *ex situ* UV/vis spectroscopy. The UV/vis spectra were recorded in diffuse reflection mode in the range of 200–600 nm using an AvaSpec-2048 fiber optic spectrometer, an AvaLight-DH-S light source by Avantes, and a glass fiber reflection probe FCR-7UV200C-2-BX-HTX. Before starting the MTO conversion, the glass fiber reflection probe was placed in the fixed-bed reactor on the top of the catalyst bed with a gap of *ca.* 1.0 mm. The reference UV/vis spectra of the catalysts were recorded at reaction temperature prior to starting the methanol flow.[38]

2.5 TGA and GC-MS analysis of organic deposits on the used low-silica AlPO-34 catalysts

The amounts of entrapped organic compounds on the low-silica AlPO-34 catalysts after the MTO conversion, performed with the time-on-stream (TOS) of 14 h, were determined by thermogravimetric analysis (TGA) using a Setram Setsys 16/18 thermogravimetric analyzer. In a typical measurement, 0.1 g of the used catalyst materials were heated in an Al_2O_3 crucible with a constant heating rate of 10 K min^{-1} and under flowing synthetic air (30 mL min^{-1}).

The nature of occluded hydrocarbons in the catalysts after the MTO conversion at TOS = 14 h was analyzed by gas chromatography-mass spectrometry (GC-MS). Typically, 0.1 g of the catalyst samples obtained after the MTO conversion were carefully dissolved in 1 M HF solution. This solution was treated with CH_2Cl_2 to extract the organic compounds, and the residual water was removed by addition of sufficient sodium sulfate. Then, 0.2 μL of the organic extract were analyzed by GC-MS (GCMS-QP2010 SE) with a RXI-5MS column (30 m, 0.25 mm i.d., stationary phase thickness 0.25 μm). The following temperature program was employed: isothermal heating at 313 K for 6 min, heating to 553 K with a rate of 10 K min^{-1}, and isothermal heating at 553 K for 10 min.

3. Results and discussion

3.1 Results of the catalyst characterization

The XRD patterns of the low-silica AlPO-34 materials before and after calcination are shown in Fig. 1. For the as-synthesized samples, the XRD patterns are typical of the triclinic chabazite (CHA) structure. The XRD patterns indicate that all samples are pure phase materials and have a high crystallinity.[49,50] After calcination, the triclinic CHA structure

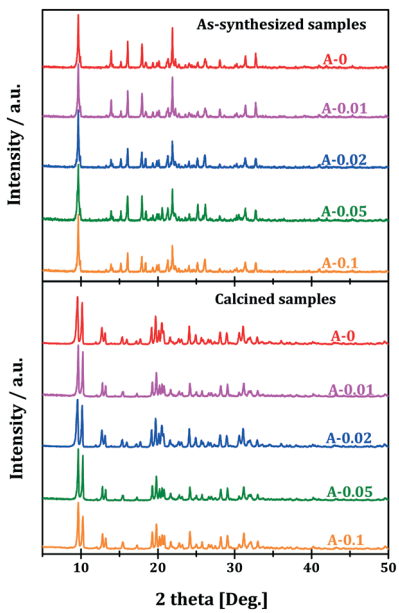

Fig. 1 XRD patterns of the as-synthesized and calcined low-silica AlPO-34 samples under study.

can be changed into the rhombohedral CHA structure, but it is dramatically distorted in the presence of water. Therefore, the XRD patterns of the low-silica AlPO-34 samples before and after calcination are strongly different, which is in agreement with those reported previously.[50] In Fig. 2, the crystal morphologies of the as-synthesized low-silica AlPO-34 samples are shown. The crystal particles of all samples have a rhombic shape, with similar crystal sizes of 10–15 μm. The chemical compositions and BET surface areas of the calcined low-silica AlPO-34 samples are given in Table 2. The molar silicon content ($n_{Si}/(n_{Al} + n_P + n_{Si})$) of the calcined samples gradually increase from 0 to 0.05 with increasing silicon content in the gel, which indicates that silicon can be introduced into AlPO-34 materials. For the A-0 sample without addition of silicon in the gel, a trace amount of silicon (0.02 mmol g^{-1}) was also determined, which originated from a silicon impurity of pseudo-boehmite.[38] The surface areas of all five low-silica AlPO-34 samples are very similar and occur in the range of 435–492 m^2 g^{-1}, which hints at the intactness and accessibility of the pore systems.

To get detailed information on the textural and acidic properties of the calcined low-silica AlPO-34 materials, multinuclear solid-state NMR spectroscopy was employed in the present study. In the ^{27}Al MAS NMR spectra, strong signals can be observed at 30–45 ppm, which are caused by tetrahedrally coordinated framework aluminum atoms, while the signals at about −15 ppm are due to octahedrally coordinated aluminum atoms (Fig. 3, left).[50–52] Additionally, much weaker signals can be observed at about 17 ppm, which are attributed to pentacoordinated aluminum atoms.[50,52] According to a previous report,[51] octahedrally coordinated and pentacoordinated aluminum atoms were caused by the deformation of the framework in the presence of water. This observation was also supported by ^{31}P MAS NMR spectroscopy. In the ^{31}P MAS NMR spectra, the dominant signals at −30 ppm are attributed to tetrahedrally coordinated phosphorus atoms in the aluminophosphate framework, while the weak signals at −22 to −26 ppm are due to the phosphorus

Table 2 Chemical compositions, specific surface areas (S_{BET}), and densities of the Brønsted acid sites (BAS) of the calcined low-silica AlPO-34 samples

Samples	Elemental analysis (mmol g^{-1})				S_{BET} (m^2 g^{-1})	BAS density[a] (mmol g^{-1})
	n_{Al}	n_P	n_{Si}	$n_{Si}/(n_{Si} + n_{Al} + n_P)$		
A-0	6.83	6.48	0.02	0	453	0.01
A-0.01	6.28	5.92	0.07	0.01	492	0.05
A-0.02	6.11	6.69	0.22	0.02	435	0.16
A-0.05	6.63	6.37	0.40	0.03	446	0.32
A-0.1	6.54	6.08	0.56	0.05	484	0.47

[a] Experimental accuracy of ±10%.

atoms neighbored to octahedrally coordinated or pentacoordinated aluminum atoms (Fig. 3, right).[50] In addition, the intensities of the above-mentioned ^{27}Al and ^{31}P MAS NMR signals are strongly decreased with the introduction of silicon, which means that the deformation of the structure can be retarded *via* the introduction of silicon atoms.

The ^{29}Si MAS NMR spectra of calcined low-silica AlPO-34 samples are dominated by signals at about −90 ppm, which are due to tetrahedrally coordinated framework silicon atoms (Fig. 4).[53] This indicates that most of the silicon atoms were successfully incorporated into the AlPO-34 framework. It is well accepted that these framework silicon species can lead to the formation of a corresponding number of bridging OH groups (Si(OH)Al), *i.e.* Brønsted acid sites.

The ^{1}H MAS NMR spectra of the calcined low-silica AlPO-34 samples are dominated by signals at 3.6 ppm due to bridging OH groups, *i.e.* Brønsted acid sites (Fig. 5, left).[54] With increasing silicon content in the samples of A-0 to A-0.1, the Brønsted acid site density, reflected by the intensities of the signals at 3.6 ppm, gradually increased. After the loading of ammonia on these samples and subsequent desorption of the physisorbed probe molecules, new signals occurred at 6.4

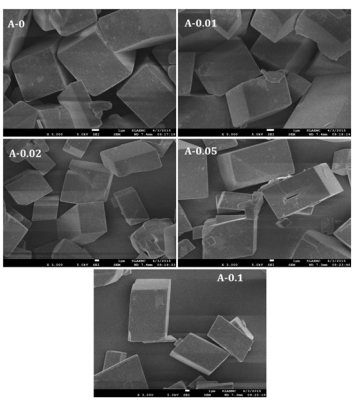

Fig. 2 SEM pictures of the as-synthesized low-silica AlPO-34 samples under study.

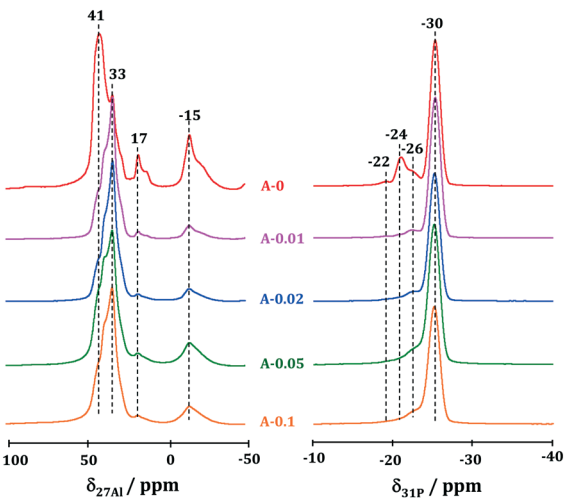

Fig. 3 ^{27}Al and ^{31}P NMR MAS NMR spectra of calcined low-silica AlPO-34 catalysts recorded in the rehydrated state.

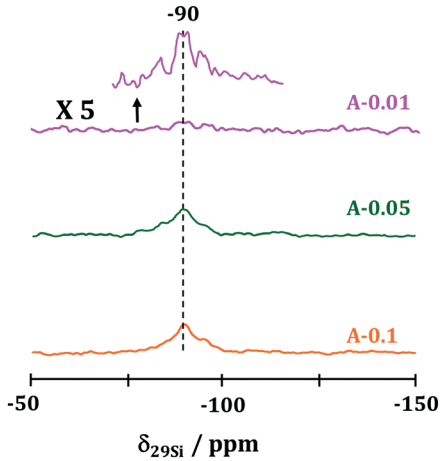

Fig. 4 ^{29}Si MAS NMR spectra of calcined low-silica AlPO-34 catalysts recorded in the rehydrated state.

ppm, which are caused by the protonation of ammonia at accessible Si(OH)Al groups leading to the formation of ammonium ions (Fig. 5, right).[55] The quantitative evaluation of these ammonium signals provided the densities of accessible Brønsted acid sites in the calcined low-silica AlPO-34 samples. The densities of accessible Brønsted acid sites were found to be 0.01, 0.05, 0.16, 0.32 and 0.47 mmol g^{-1} for the A-0, A-0.01, A-0.02, A-0.05, and A-0.1 samples, respectively (Table 2). Compared with the results of elemental analysis, this finding means that most of the silicon atoms were successfully introduced into the framework of the AlPO-34 samples and caused the formation of bridging OH groups (Si(OH)Al). Additional weak ^{1}H MAS NMR signals at 0.2 to 2.4 ppm, which were observed before and after ammonia loading on the AlPO-34 samples, are due to non-acidic POH and AlOH groups at the framework defects and the outer crystal surfaces.[54]

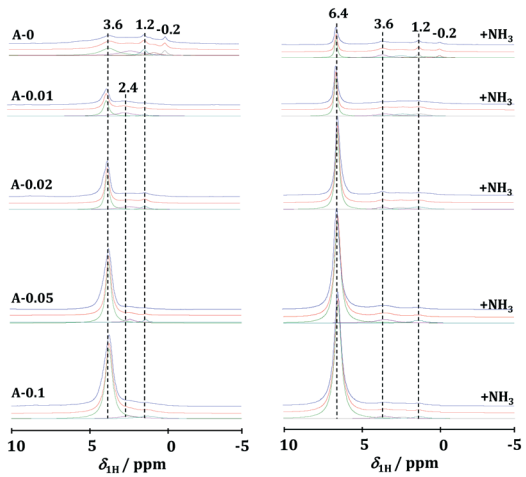

Fig. 5 ^{1}H MAS NMR spectra of the calcined low-silica AlPO-34 samples recorded before (left) and after (right) adsorption of ammonia. From top to bottom, the experimental spectra, the simulated spectra, and the signal components utilized for simulation are shown.

3.2 Catalytic performance of the low-silica AlPO-34 catalysts in the MTO conversion

In Fig. 6a, the curves for the methanol conversion over the low-silica AIPO-34 catalysts are shown. It is obvious that the density of the Brønsted acid site has a strong impact on the catalytic activity and lifetime of the MTO catalysts under study. For the A-0 and A-0.01 catalysts with the low Brønsted acid site densities of 0.01 and 0.05 mmol g^{-1}, the initial methanol conversions at a time-on-stream (TOS) of 15 min are 82.7% and 96.5%, respectively. However, with an increasing TOS, the methanol conversion gradually decreased and dropped to nearly 0% at TOS = 14 h. With increasing Brønsted acid site density, however, an initial methanol conversion of 100% can be reached for the A-0.02, A-0.05, and A-0.1 catalysts, while the lifetimes of these catalysts are increased first and, thereafter, decreased. For the A-0.05 catalyst with the optimum Brønsted acid site density of 0.32 mmol g^{-1}, a catalyst lifetime of 15 h with a methanol conversion of >99% could be achieved, which is much better than that of SAPO-34 catalysts under similar reaction conditions (Table 3).[18,56,57] After regeneration of the used A-0.05 catalyst, the catalytic performance could be fully recovered (Fig. 6b), which indicates that carbon deposits are responsible for the catalyst deactivation.

The time dependence of the product selectivity of the low-silica AlPO-34 catalysts during the MTO conversion is shown in Fig. 7. For all the five samples, small olefins ($C_2^{=}$–$C_4^{=}$) are the main product molecules (70–85%) in the initial period of the MTO conversion, which indicates that the MTO

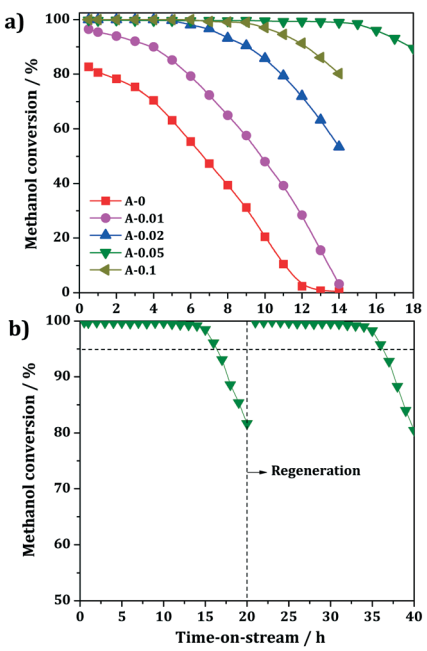

Fig. 6 MTO conversion plotted as a function of time-on-stream on the low-silica AlPO-34 samples with different Brønsted acid site densities (a) and catalytic properties of generated A-0.05 catalysts used as MTO catalysts at 673 K (b).

Table 3 Catalyst lifetime and product selectivity during the MTO conversion over A-0.05 and different SAPO-34 catalysts[a]

Sample	Lifetime (min)	$C_2^= + C_3^=$ (%)	Ref.
AlPO-34 (A-0.05)	900	83	Present work
SAPO-34 (small crystal sizes)	600	80	18
Hierarchical SAPO-34[b]	≈500	82	56
Plate-like SAPO-34[c]	600	83	57

[a] Experimental conditions: T = 673 K, WHSV ≈ 1.0 h^{-1}. The catalyst lifetime is defined as the reaction duration with >99% methanol conversion. The highest selectivity of ethene and propene under 99% methanol conversion. [b] The WHSV used in ref. 56 is 0.73 h^{-1}. [c] The WHSV used in ref. 57 is 1.2 h^{-1}.

conversion can be successfully realized over all the low-silica AlPO-34 samples with different Brønsted acid site densities. With further progress of the MTO conversion, the product distributions of these catalysts strongly varied.

Interestingly, for the A-0 and A-0.01 catalysts with low Brønsted acid site densities of 0.01 and 0.05 mmol g^{-1}, respectively, besides the main products consisting of $C_2^=$–$C_4^=$ olefins, a higher selectivity to $C_5^=$–$C_6^=$ olefins of >20% was obtained in the initial period of the MTO conversion. With increasing TOS, the selectivity to these long-chain alkenes decreased first and, thereafter, increased gradually. Meanwhile, the variation trend of the selectivity to $C_2^=$–$C_3^=$ olefins is exactly in the opposite direction. According to previous studies,[21,28] this may result from the olefin methylation–cracking route, *i.e.* the olefin-based cycle mechanism. On one side, the long-chain alkenes can be cracked to lower olefins ($C_2^=$–$C_3^=$). On the other side, these long-chain alkenes can also be converted to larger compounds, *e.g.*, dienes or aromatics. Therefore, with the decrease of the selectivity to $C_5^=$–$C_6^=$ olefins, the selectivity to $C_2^=$–$C_3^=$ olefins gradually increased. However, with the deactivation of the A-0 catalyst, the selectivity to $C_2^=$–$C_3^=$ olefins started to decrease, while the selectivity to $C_5^=$–$C_6^=$ olefins gradually increased simultaneously. This finding indicates that the cracking or methylation of the long-chain alkenes is suppressed because of the deactivation of the catalyst. Therefore, these large alkenes can freely diffuse out of the cages of the AlPO-34 catalysts. In addition, with the increase of the Brønsted acid density of the AlPO-34 catalysts, the initial selectivity to $C_5^=$–$C_6^=$ olefins gradually decreased, while the selectivity to lower olefins ($C_2^=$–$C_4^=$) started to increase. This means that the long-chain alkenes can be rapidly cracked to smaller olefins according to the cracking route or be quickly converted to large organic compounds *via* the methylation route over the catalysts with higher Brønsted acid site densities. This means that the MTO catalytic performance of the low-silica AlPO-34 catalysts under study and the contribution of the dual-cycle mechanism during the MTO conversion can be modified to some extent by changing the Brønsted acid site density.

In order to get further information about the initial period of the MTO conversion, the A-0 catalyst was selected as a

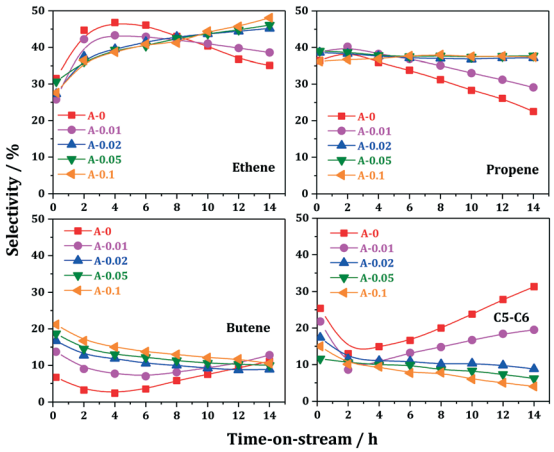

Fig. 7 Product distribution observed for the MTO conversion over the low-silica AlPO-34 catalysts under study with different Brønsted acid site densities.

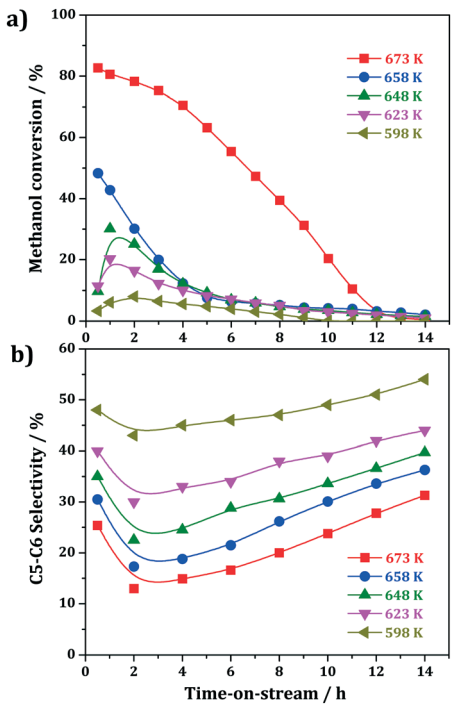

Fig. 8 Methanol conversion (a) and selectivity of C_5–C_6 alkenes (b) over A-0 at different reaction temperatures as a function of TOS.

model catalyst and investigated in the MTO conversion at low reaction temperatures in the range of 598–673 K. As shown in Fig. 8a, when the reaction temperature was decreased from 673 K to 658 K, the initial methanol conversion rapidly decreased from 82.7% to 48.3%. With the further decrease of the reaction temperature, the initial methanol conversion gradually dropped to lower than 10%, and an induction period could be obviously observed. Meanwhile, the selectivity to $C_5^=$–$C_6^=$ olefins gradually increased from 25% to nearly 50% (Fig. 8b). These results clearly indicate that the olefin-based mechanism is the dominant reaction mechanism in the initial period of the MTO conversion over the A-0 catalyst with a low Brønsted acid site density.

3.3 TGA and GC-MS analysis of organic deposits on the used low-silica AlPO-34 catalysts

To quantify the organic deposits formed on the different low-silica AlPO-34 catalysts after the MTO conversion at TOS = 14 h, the total weights of organic deposits formed on A-0, A-0.01, A-0.02, A-0.05 and A-0.1 were determined by TGA in the temperature range of 298 K to 973 K. According to Fig. 9, two obvious weight losses can be recognized: a low-temperature weight loss at <373 K and a high-temperature weight loss at >673 K, which are ascribed to desorption of water and occluded coke compounds, respectively. Similar weight losses of adsorbed water (6.0–7.5 wt%) could be observed for all used catalysts in the low-temperature range (<373 K). In contrast, in the high-temperature range (>673 K), the weight loss of the used catalysts correlates well with the Brønsted acid density, and the coke amount increases from 4.5 wt% to 16.1 wt%. This indicates that organic compounds rapidly accumulate on low-silica AlPO-34 catalysts with higher Brønsted acid site densities.

To consider the coke formation over the used catalysts with different Brønsted acid site densities in more detail, the average coke formation rate (R_{coke}) and the fraction of methanol consumed for coke formation (W_{coke}) were evaluated and are given in Table 4, columns 3 and 4, respectively. Furthermore, the coke formation per Brønsted acid site (M_{coke}) is given in column 5. The above-mentioned values were calculated according to:

$$R_{coke}(\text{g min}^{-1}) = \text{coke amount (g)/reaction time (min)}$$

$$W_{coke}(\text{g g}^{-1}) = \text{coke amount (g)/methanol feedstock (g)}$$

$$M_{coke}(\text{g}^2\ \text{mmol}^{-1}) = \text{coke amount (g)/Brønsted acid sites (mmol g}^{-1})$$

Table 4 Coke amount, average coke formation rate (R_{coke}), fraction of the methanol consumed for the coke formation (W_{coke}), and coke formation per Brønsted acid site (M_{coke}) during the MTO conversion over the low-silica AlPO-34 catalysts under study, determined for TOS = 14 h

Catalysts	Coke (wt%)	R_{coke} (mg min^{-1})	W_{coke} (g g^{-1})	M_{coke} (g^2 mmol^{-1})
A-0	4.5	0.021	0.007	4.5
A-0.01	6.8	0.032	0.008	1.4
A-0.02	11.6	0.055	0.009	0.7
A-0.05	12.2	0.057	0.009	0.4
A-0.1	16.1	0.077	0.012	0.3

The coke amounts, the coke formation rates, and the fractions of methanol consumed for the coke formation in Table 4 show a gradual increase with increasing Brønsted acid density for the catalysts A-0 to A-0.1. In contrast, the average coke formation per Brønsted acid site varies in the opposite direction. Even the coke amount formed on A-0.02 (11.6 wt%) is close to that formed on A-0.05 (12.2 wt%). Typically, the similar slopes of the conversion *versus* time on stream curves in Fig. 6 may indicate that the main difference between the low-silica AlPO-34 catalysts could not be the different deactivation rates (Table 4, column 2), but rather the number of Brønsted acid sites which are active in the MTO reaction under the present reaction conditions.[58] On the other hand, for the catalyst with a slightly lower Brønsted acid site density, *i.e.* A-0.02, a much higher M_{coke} was found. This means that the rapid coverage of Brønsted acid sites by coke may be the main reason for the deactivation of A-0 with the lowest Brønsted acid site density. In contrast, for A-0.1 with a higher Brønsted acid site density, the pore blockage by the large coke compounds should be the main reason for the catalyst deactivation. On the other hand, A-0.05 with the most suitable Brønsted acid site density can well balance the coke formation rate, and therefore, exhibit the best catalyst stability in the MTO conversion.

The chemical composition of the organic deposits occluded in the used low-silica AlPO-34 catalysts was analyzed by GC-MS and the results are shown in Fig. 10. Polymethylnaphthalenes with one to two fused aromatic rings are detected in all used catalysts, while large polycyclic aromatics with three to four condensed aromatic rings were exclusively observed for the A-0.1 catalyst. Typically, tetramethylbenzene molecules are the dominant components

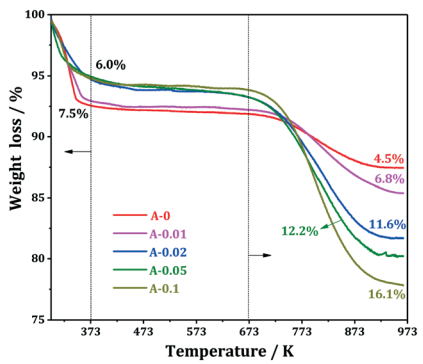

Fig. 9 TGA curves of used low-silica AlPO-34 catalysts obtained after MTO conversion at the reaction temperature of 673 K and at TOS = 14 h.

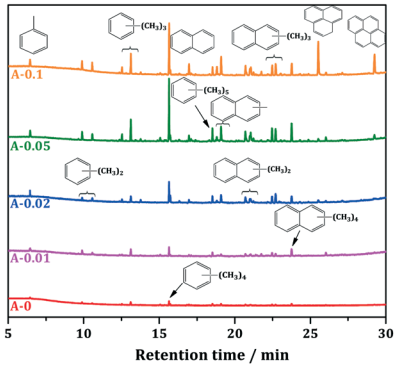

Fig. 10 GC-MS chromatograms of the organic extracts from used low-silica AlPO-34 catalysts obtained after the MTO conversion at the reaction temperature of 673 K and TOS = 14 h.

among the polymethylbenzenes. Additionally, the concentrations of these organic deposits, reflected as the intensities of the GC-MS signals, changed strongly with increasing Brønsted acid site densities, which fits well with the TGA results. On the basis of these observations, it can be concluded that larger organic compounds, like anthracene and phenanthrene, more rapidly accumulate on catalysts with a higher Brønsted acid site density and *vice versa*. Therefore, the probability of pore-blocking as a reason for the deactivation of the A-0.05 and A-0.1 catalysts is much higher than that for the A-0 and A-0.01 catalysts, which also agrees with the TGA results.

3.4 UV/vis studies of intermediates formed during the MTO conversion over low-silica AlPO-34 catalysts

The chemical composition of the occluded aromatics was obtained by the above-mentioned GC-MS studies (Fig. 10), while the detailed chemical nature, *e.g.* the occurrence of dienes and carbenium ions, could not be given by this method. Therefore, UV/vis spectroscopy was utilized to investigate the nature of the organic deposits on the used low-silica AlPO-34 catalysts. In Fig. 11, the *ex situ* UV/vis spectra of the used low-silica AlPO-34 catalysts recorded at 673 K and TOS = 14 h are shown. For all five low-silica AlPO-34 catalysts, similar UV/vis bands at ~230, 285, 335, 350, 415 and 495 nm occurred after TOS = 14 h. According to previous studies,[39,59–64] the band at 230 nm was assigned to UV/vis-sensitive dienes, while the bands at *ca.* 285 nm are due to aromatic species or monoenylic carbenium ions. The bands at 335–350 and 415 nm can be attributed to dienylic carbenium ions and polycyclic aromatics.[60] The latter species are formed with two or three condensed aromatic rings and occur at wavelengths lower than 400 nm, while those formed with four condensed aromatic rings occur at wavelengths slightly higher than 400 nm.[63] Broad UV/vis bands occurring at ~495 nm hint at the formation of trienylic carbenium ions.[60] The amount of UV/vis-sensitive organic species deposited on the used low-silica AlPO-34 catalysts changes strongly with the Brønsted acid site density, as indicated by their band intensities in Fig. 11. The diene content (230 nm) decreases strongly with increasing Brønsted acid site density. In contrast, the aromatic species (~285 nm) and polycyclic aromatics (~415 nm) contents increase with increasing Brønsted acid site density, which agrees very well with the high-temperature weight loss determined by TGA (Fig. 9, right) and the distribution of aromatics observed by GC-MS (Fig. 10).

The nature of the organic compounds formed during the MTO conversion over the A-0 and A-0.1 catalysts with low and high Brønsted acid densities, respectively, was also monitored by *in situ* UV/vis spectroscopy at 673 K. Fig. 12 shows the UV/vis spectra of the organic species formed on the A-0 and A-0.1 catalysts during the MTO conversion at TOS = 14 h. All the above-mentioned organic species can be rapidly formed during the initial TOS = 0.5 h, and their intensities gradually increased with the progress of the MTO conversion. Interestingly, the amounts of the intermediates don't change

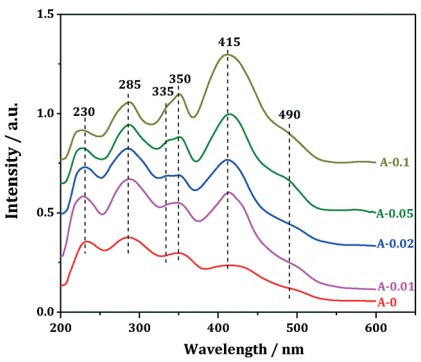

Fig. 11 *Ex situ* UV/vis spectra of low-silica AlPO-34 catalysts obtained after the MTO conversion at the reaction temperature of 673 K and for TOS = 14 h.

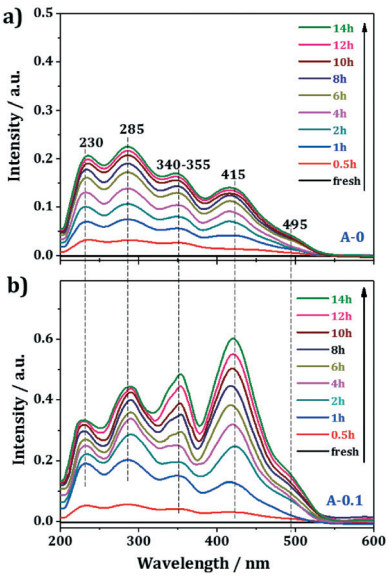

Fig. 12 *In situ* UV/vis spectra recorded during the MTO conversion over A-0 (a) and A-0.1 (b) at 673 K and up to TOS = 14 h.

significantly during the MTO conversion over the A-0 catalyst. For the A-0.1 catalyst, the polycyclic aromatics appearing at 415 nm rapidly became the dominant species. This means that the polycyclic aromatics can rapidly accumulate on the catalysts with high Brønsted acid site densities. In addition, it can be noted that the distribution and proportions of the intermediates formed during the initial TOS = 1.0 h over the A-0.1 catalyst are very similar to those on the A-0 catalyst. This indicates that the olefin-based cycle mechanism should be the dominant mechanism in the initial period of the MTO conversion both on the A-0 catalyst and the A-0.1 catalyst. However, with the progress of the MTO conversion, namely, during the steady-state, the aromatic-based cycle mechanism becomes the dominant mechanism over the A-0.1 catalyst with a high Brønsted acid site density.

In Fig. 13a, the UV/vis spectra recorded at different reaction temperatures (598–673 K) over the A-0 catalyst at TOS = 14 h are compared. With a decreasing reaction temperature, the amounts of aromatic species (275–285 nm), dienylic carbenium ions (340–360 nm), and polycyclic aromatics (415 nm) gradually decrease, while dienes (215–234 nm) become the dominant organic compounds. Interestingly, when the reaction temperature decreased to 598 K, nearly no UV/vis bands of aromatics could be observed – only those of dienes. Hence, at this reaction temperature, the catalyst already exhibits MTO activity. Further *in situ* UV/vis spectra recorded at 598 K clearly indicate that dienes are the dominant organic species during the induction period of the MTO conversion, while nearly no aromatics could be observed (Fig. 13b). This means that the formation of aromatics is totally suppressed and the olefin-based cycle mechanism is the dominant mechanism of the MTO conversion. Long-chain alkenes, *e.g.*, $C_5^{=}$–$C_6^{=}$ olefins, can act as active hydrocarbons and are cracked to small olefins, and can also diffuse out of the cages of the catalyst, allowing their detection as reaction products. Simultaneously, these long-chain alkenes can also be converted to dienes, which are another kind of catalytically active hydrocarbons.

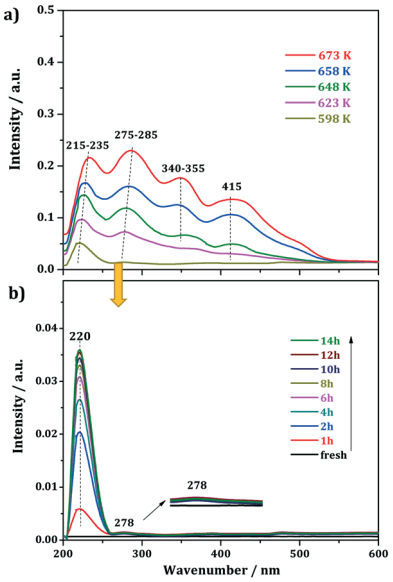

Fig. 13 *Ex situ* UV/vis spectra of A-0 recorded after the MTO conversion at different reaction temperatures and TOS = 14 h (a), and *in situ* UV/vis spectra recorded during the MTO conversion over A-0 at the reaction temperature of 598 K and up to TOS = 14 h (b).

3.5 Reaction mechanism of the MTO conversion on low-silica AlPO-34 catalysts

In the MTO conversion, Brønsted acid sites play a key role as catalytically active sites. Therefore, low-silica AlPO-34 materials with similar crystal sizes but different Brønsted acid site densities in the range of 0.01–0.47 mmol g^{-1} (A-0 to A-0.1) were applied as MTO catalysts. The present work focused on the effect of the Brønsted acid site density on the catalytic properties and reaction mechanism during the MTO conversion, which was investigated *via* several methods, such as TGA, GC-MS, and *ex situ*/*in situ* UV/vis spectroscopy.

As demonstrated by UV/vis spectroscopy, dienes and polymethylbenzenes are the dominant intermediates on the A-0 and A-0.01 catalysts with low Brønsted acid site densities (Fig. 11). Interestingly, for the A-0 catalyst and a reaction temperature of 598 K accompanied by a low MTO activity, dienes are the dominant organic compounds, and nearly no aromatics could be observed. According to these observations, it can be concluded that the olefin methylation and cracking route, *i.e.* the olefin-based cycle mechanism, plays a key role during the early stages of the MTO reaction on low-silica AlPO-34 catalysts. As shown in Scheme 1, long-chain alkenes are probably formed *via* the methylation of olefins, can act as the main active hydrocarbons, and are cracked to lower olefins. Some of these alkenes with straight chains (marked in red in Scheme 1) can also diffuse out of the catalyst cages and are detected as reaction products. These long-chain alkenes can be further methylated and converted to dienes, which are UV/vis-sensitive and give an UV/vis band at about 220 nm. With further progress of the MTO conversion, dienes can be converted to other larger organic compounds, such as aromatics (285 nm) and dienylic carbenium ions (340–360 nm). Then, an aromatic-based cycle starts to participate during the steady-state of the MTO conversion. For the low-silica

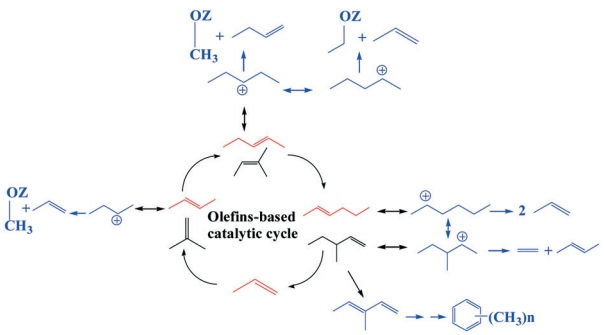

Scheme 1 Olefin-based cycle mechanism in the MTO conversion over low-silica AlPO-34 catalysts.

AlPO-34 catalysts with lower Brønsted acid site densities, the aromatic-based cycle can be strongly suppressed and the olefin-based cycle plays an important role during the initial stages of the MTO conversion, and long-chain $C_5^=$–$C_6^=$ alkenes can act as active hydrocarbon pool species. With decreasing reaction temperatures, the methylation route was much more favored than the cracking route. Therefore, higher selectivities to $C_5^=$–$C_6^=$ alkenes (~50%) could be achieved in the product flow (Fig. 8b). Simultaneously, dienes are the dominant deposits occluded in the used catalysts. With increasing Brønsted acid site densities of the catalysts, the dominant olefin-based cycle mechanism was gradually replaced by the aromatic-based cycle mechanism. Hence, the selectivity to $C_5^=$–$C_6^=$ alkenes in the products was gradually decreased (Fig. 7), while larger organic deposits, such as aromatics, rapidly accumulated and were occluded in the catalyst pores and cages, which is also supported by TGA (Fig. 9), GC-MS (Fig. 10), and UV/vis measurements (Fig. 11).

A comparison of the deactivation behavior of all low-silica AlPO-34 catalysts under study indicates that the reasons for the deactivation vary with changing Brønsted acid density. For the A-0.1 catalyst with the highest Brønsted acid site density, the largest coke amount, the highest coke formation rate, and the largest fraction of methanol consumed for coke formation are accompanied by the aromatic-based cycle as the dominant reaction mechanism during the MTO conversion. Therefore, large coke compounds consisting of polycyclic aromatics rapidly accumulated and were occluded in the used catalysts (GC-MS), which leads to pore blockage, causing the catalyst deactivation. With decreasing Brønsted acid site density, the coke formation rate and the formation of polycyclic aromatics can be gradually suppressed, and the olefin-based mechanism becomes dominant. Simultaneously, the coke formation per BAS (M_{coke}) increases strongly. Therefore, *e.g.*, the few Brønsted acid sites of the A-0 catalyst can be rapidly covered by coke species, which explains the catalyst deactivation in this case. Additionally, with the decrease of the Brønsted acid site density, the MTO activity of the catalysts becomes lower, and the methylation route in the olefin-based cycle is much more favored than the cracking route. Therefore, a lower catalyst lifetime and a higher selectivity to $C_5^=$–$C_6^=$ alkenes were obtained for A-0.01 and A-0. Typically, the A-0.05 catalyst with the optimum Brønsted acid site density of 0.32 mmol g^{-1} can well balance the two reaction cycles and the deactivation rate and, therefore, exhibits the longest catalyst lifetime of up to TOS = 15 h.

4. Conclusion

In the present work, low-silica AlPO-34 materials with similar crystal sizes of 10–15 μm but different Brønsted acid site densities in the range of 0.01–0.47 mmol g^{-1} were prepared and applied as catalysts in the MTO conversion. To elucidate the effect of the Brønsted acid density of low-silica AlPO-34 catalysts on their catalytic properties and the dominant reaction mechanism during the MTO conversion, several methods, such as TGA, GC-MS, solid-state NMR spectroscopy, and *ex situ*/*in situ* UV/vis spectroscopy were employed.

For the low-silica AlPO-34 catalysts with low Brønsted acid site densities, the olefin-based cycle mechanism is the dominant mechanism during the MTO conversion. Long-chain alkenes, *e.g.*, $C_5^=$–$C_6^=$ alkenes, can act as the main catalytically active hydrocarbons, which are cracked to smaller olefins, and of which some with a straight chain can diffuse out of the cages of the catalyst and are directly detected as the main reaction products. Simultaneously, the long-chain alkenes can also be converted to dienes, which was monitored by UV/vis spectroscopy. With increasing Brønsted acid site density, these alkenes are rapidly transferred to large organic compounds, *e.g.*, polymethylbenzenes and polycyclic aromatics, and the aromatic-based cycle mechanism becomes the dominant mechanism. Additionally, the accumulation of polycyclic aromatics on the low-silica AlPO-34 catalysts with high Brønsted acid site densities can cause rapid deactivation of the catalysts. Interestingly, the A-0.05 catalyst with the optimum Brønsted acid site density of 0.32 mmol g^{-1} is able to well balance the catalyst activity and deactivation and, therefore, exhibits the longest lifetime of 15 h.

Acknowledgements

This work was financially supported by the National Natural Science Foundation of China (21303089, 21303087, and 21421001), the Municipal Natural Science Foundation of Tianjin (13JCQNJC05900, 13RCGFGX01124, and 14JCQNJC05700), and the Ministry of Education of China (IRT-13022). Furthermore, M. H. wants to thank the Deutsche Forschungsgemeinschaft for financial support (HU533/13-1).

References

1 M. Stoecker, in *Zeolite and Catalysis: Synthesis, Reactions and Applications*, ed. J. Čejka, A. Corma and S. Zones, Wiley-VCH, Weinheim, 2010, p. 687.
2 U. Olsbye, S. Svelle, M. Bjørgen, P. Beato, T. V. W. Janssens, F. Joensen, S. Bordiga and K. P. Lillerud, *Angew. Chem., Int. Ed.*, 2012, **51**, 5810–5831.
3 K. Hemelsoet, J. Mynsbrugge, K. Wispelaere, M. Waroquier and V. Speybroeck, *ChemPhysChem*, 2013, **14**, 1526–1545.
4 S. Ilias and A. Bhan, *ACS Catal.*, 2013, **3**, 18–31.
5 P. Tian, Y. X. Wei, M. Ye and Z. M. Liu, *ACS Catal.*, 2015, **5**, 1922–1938.
6 U. Olsbye, S. Svelle, K. P. Lillerud, Z. H. Wei, Y. Y. Chen, J. F. Li, J. G. Wang and W. B. Fan, *Chem. Soc. Rev.*, 2015, **44**, 7155–7176.
7 S. Teketel, W. Skistad, S. Benard, U. Olsbye, K. P. Lillerud, P. Beato and S. Svelle, *ACS Catal.*, 2012, **2**, 26–37.
8 Y. Bhawe, M. Moliner-Marin, J. D. Lunn, Yu. Liu, A. Malek and M. Davis, *ACS Catal.*, 2012, **2**, 2490–2495.
9 M. Yoshioka, T. Yokoi and T. Tatsumi, *ACS Catal.*, 2015, **5**, 4268–4275.

10 E. Borodina, F. Meirer, I. Lezcano-González, M. Mokhtar, A. M. Asiri, S. A. Al-Thabaiti, S. N. Basahel, J. Ruiz-Martinez and B. M. Weckhuysen, *ACS Catal.*, 2015, **5**, 992–1003.
11 X. C. Zhu, J. P. Hofmann, B. Mezari, N. Kosinov, L. L. Wu, Q. Y. Qian, B. M. Weckhuysen, S. Asahina, J. Ruiz-Martínez and E. J. M. Hensen, *ACS Catal.*, 2016, **6**, 2163–2177.
12 J. Z. Li, Y. X. Wei, J. R. Chen, P. Tian, X. Su, S. T. Xu, Y. Qi, Q. Y. Wang, Y. Zhou, Y. L. He and Z. M. Liu, *J. Am. Chem. Soc.*, 2012, **134**, 836–839.
13 I. M. Dahl and S. Kolboe, *J. Catal.*, 1994, **149**, 304–309.
14 I. M. Dahl and S. Kolboe, *J. Catal.*, 1996, **161**, 458–464.
15 B. Arstad and S. Kolboe, *J. Am. Chem. Soc.*, 2001, **123**, 8137–8138.
16 W. G. Song, J. F. Haw, J. B. Nicholas and C. S. Henegha, *J. Am. Chem. Soc.*, 2000, **122**, 10726–10727.
17 J. F. Haw, W. G. Song, D. M. Marcus and J. B. Nicholas, *Acc. Chem. Res.*, 2003, **36**, 317–326.
18 W. L. Dai, G. J. Wu, L. D. Li, N. J. Guan and M. Hunger, *ACS Catal.*, 2013, **3**, 588–596.
19 Y. Y. Chen, Z. H. Wei, S. Wang, J. F. Li, M. Dong, Z. F. Qin, J. G. Wang, H. J. Jiao and W. B. Fan, *Catal. Sci. Technol.*, 2016, **6**, 5326–5335.
20 S. Svelle, F. Joensen, J. Nerlov, U. Olsbye, K. P. Lillerud, S. Kolboe and M. Bjørgen, *J. Am. Chem. Soc.*, 2006, **128**, 14770–14771.
21 M. Bjørgen, S. Svelle, F. Joensen, J. Nerlov, S. Kolboe, F. Bonino, L. Palumbo, S. Bordiga and U. Olsbye, *J. Catal.*, 2007, **249**, 195–207.
22 D. Lesthaeghe, J. Mynsbrugge, M. Vandichel, M. Waroquier and V. Speybroeck, *ChemCatChem*, 2011, **3**, 208–212.
23 S. Ilias and A. Bhan, *J. Catal.*, 2012, **290**, 186–192.
24 A. Hwang, D. Prieto-Centurion and A. Bhan, *J. Catal.*, 2016, **337**, 52–56.
25 X. Y. Sun, S. Mueller, H. Shi, G. L. Haller, M. Sanchez-Sanchez, A. C. Veen and J. A. Lercher, *J. Catal.*, 2014, **314**, 21–31.
26 X. Y. Sun, S. Mueller, Y. Liu, H. Shi, G. L. Haller, M. Sanchez-Sanchez, A. C. Veen and J. A. Lercher, *J. Catal.*, 2014, **317**, 185–197.
27 C. M. Wang, Y. D. Wang and Z. K. Xie, *Catal. Sci. Technol.*, 2014, **4**, 2631–2638.
28 C. M. Wang, Y. D. Wang and Z. K. Xie, *J. Catal.*, 2013, **301**, 8–19.
29 Y. Y. Chu, X. Y. Sun, X. F. Yi, L. H. Ding, A. M. Zheng and F. Deng, *Catal. Sci. Technol.*, 2015, **5**, 3507–3517.
30 C. Wang, J. Xu, G. D. Qi, Y. J. Gong, W. Y. Wang, P. Gao, Q. Wang, N. D. Feng, X. L. Liu and F. Deng, *J. Catal.*, 2015, **332**, 127–137.
31 S. Wang, Y. Y. Chen, Z. F. Wei, Z. F. Qin, H. Ma, M. Dong, J. F. Li, W. B. Fan and J. G. Wang, *J. Phys. Chem. C*, 2015, **119**, 28482–28498.
32 S. Wang, Z. H. Wei, Y. Y. Chen, Z. F. Qin, H. Ma, M. Dong, W. B. Fan and J. G. Wang, *ACS Catal.*, 2015, **5**, 1131–1144.
33 Z. M. Cui, Q. Liu, W. G. Song and L. J. Wan, *Angew. Chem., Int. Ed.*, 2006, **45**, 6512–6515.
34 Z. M. Cui, Q. Liu, Z. Ma, S. W. Bian and W. G. Song, *J. Catal.*, 2008, **258**, 83–86.
35 F. F. Wei, Z. M. Cui, X. J. Meng, C. Y. Cao, F. S. Xiao and W. G. Song, *ACS Catal.*, 2014, **4**, 529–534.
36 J. H. Ahn, B. Temel and E. Iglesia, *Angew. Chem.*, 2009, **121**, 3872–3874.
37 D. A. Simonetti, J. H. Ahn and E. Iglesia, *J. Catal.*, 2011, **277**, 173–195.
38 W. L. Dai, C. M. Wang, M. Dyballa, G. J. Wu, N. J. Guan, L. D. Li, Z. K. Xie and M. Hunger, *ACS Catal.*, 2015, **5**, 317–326.
39 W. L. Dai, M. Dyballa, G. J. Wu, L. D. Li, N. J. Guan and M. Hunger, *J. Phys. Chem. C*, 2015, **119**, 2637–2645.
40 M. W. Erichsen, S. Svelle and U. Olsbye, *J. Catal.*, 2013, **298**, 94–101.
41 M. W. Erichsen, K. Wispelaere, K. Hemelsoet, S. L. C. Moors, T. Deconinck, M. Waroquier, S. Svelle, V. Speybroeck and U. Olsbye, *J. Catal.*, 2015, **328**, 186–196.
42 W. L. Dai, X. Wang, G. J. Wu, L. D. Li, N. J. Guan and M. Hunger, *ChemCatChem*, 2012, **4**, 1428–1435.
43 S. Wilson and P. Barger, *Microporous Mesoporous Mater.*, 1999, **29**, 117–126.
44 I. M. Dahl, H. Mostad, D. Akporiaye and R. Wendelbo, *Microporous Mesoporous Mater.*, 1999, **29**, 185–190.
45 A. Izadbakhsh, F. Farhadi, F. Khorasheh, S. Sahebdelfar, M. Asadi and Z. F. Yan, *Appl. Catal., A*, 2009, **364**, 48–56.
46 T. Alváro-Munoz, C. Márquez-Alvárez and E. Sastre, *Catal. Today*, 2013, **213**, 219–225.
47 L. Xu, A. P. Du, Y. X. Wei, Y. L. Wang, Z. X. Yu, Y. L. He, X. Z. Zhang and Z. M. Liu, *Microporous Mesoporous Mater.*, 2012, **152**, 178–184.
48 W. L. Dai, N. Li, L. D. Li, N. J. Guan and M. Hunger, *Catal. Commun.*, 2011, **16**, 124–127.
49 L. Marchese, A. Frache, E. Gianotti, G. Martra, M. Causá and S. Coluccia, *Microporous Mesoporous Mater.*, 1999, **30**, 145–153.
50 A. Tuel, S. Caldarelli, A. Meden, L. B. McCusker, C. Baerlocher, A. Ristic, N. Rajic, G. Mali and V. Kaucic, *J. Phys. Chem. B*, 2000, **104**, 5697–5705.
51 G. Poulet, A. Tuel and P. Sautet, *J. Phys. Chem. B*, 2005, **109**, 22939–22946.
52 J. Varlec, A. Krajnc, M. Mazaj, A. Ristić, K. Vanatalu, A. Oss, A. Samoson, V. Kaučič and G. Mali, *New J. Chem.*, 2016, **40**, 4178–4186.
53 W. L. Dai, X. Wang, G. J. Wu, N. J. Guan, M. Hunger and L. D. Li, *ACS Catal.*, 2011, **1**, 292–299.
54 Y. Jiang, J. Huang, W. Dai and M. Hunger, *Solid State Nucl. Magn. Reson.*, 2011, **39**, 116–141.
55 W. L. Dai, M. Scheibe, N. J. Guan, L. D. Li and M. Hunger, *ChemCatChem*, 2011, **3**, 1130–1133.
56 X. Liu, S. Ren, G. F. Zeng, G. J. Liu, P. Wu, G. Wang, X. Q. Chen, Z. Y. Liu and Y. H. Sun, *RSC Adv.*, 2016, **6**, 28787–28791.
57 T. Álvaro-Muñoz, E. Sastre and C. Márquez-Álvarez, *Catal. Sci. Technol.*, 2014, **4**, 4330–4339.
58 B. P. C. Hereijgers, F. Bleken, M. H. Nilsen, S. Svelle, K.-P. Lillerud, M. Bjørgen, B. M. Weckhuysen and U. Olsbye, *J. Catal.*, 2009, **264**, 77–87.

59 N. C. Deno, J. Bollinger, N. Friedman, K. Hafer, J. D. Hodge and J. J. Houser, *J. Am. Chem. Soc.*, 1963, **85**, 2998–3000.
60 I. Kiricsi, H. Fcrster, G. Tasi and J. B. Nagy, *Chem. Rev.*, 1999, **99**, 2085–2114.
61 Y. J. Jiang, J. Huang, V. R. R. Marthala, Y. Ooi, J. Weitkamp and M. Hunger, *Microporous Mesoporous Mater.*, 2007, **105**, 132–139.
62 M. Bjørgen, F. Bonino, S. Kolboe, K.-P. Lillerud, A. Zecchina and S. Bordiga, *J. Am. Chem. Soc.*, 2003, **125**, 15863–15868.
63 H. G. Karge, M. Laniecki, M. Ziolek, G. Onyestyak, A. Kiss, P. Kleinschmit and M. Siray, in *Zeolites: Facts, Figures, Future*, 8th International Zeolite Conference, Amsterdam, Netherlands, 1989; *Studies in Surface Science and Catalysis*, ed. P. A. Jacobs and R. A. van Santen, Elsevier, Amsterdam, 1989, vol. 49, p. 1327.
64 J. W. Park, J. Y. Lee, K. S. Kim, S. B. Hong and G. Seo, *Appl. Catal., A*, 2008, **339**, 36–44.